The Effect of Water-Induced Stress To Enhance Hydrocarbon Recovery in Shale Reservoirs

Perapon Fakcharoenphol, Sarinya Charoenwongsa, Hossein Kazemi, and **Yu-Shu Wu,** Colorado School of Mines

Summary

Waterflooding has been an effective improved-oil-recovery (IOR) process for several decades. However, stress induced by waterflooding has not been well studied or documented. Water injection typically increases reservoir pressure and decreases reservoir temperature. The increase in reservoir pressure and decrease in reservoir temperature synergistically reduce the effective stress. Because of such decrease in stress, existing healed natural fractures can be reactivated and/or new fractures can be created. Similar effects can enhance hydrocarbon recovery in shale reservoirs.

In this paper, we calculated the magnitude of water-injection-induced stress with a coupled flow/geomechanics model. To evaluate the effect of water injection in the Bakken, a numerical-simulation study for a sector model was carried out. Stress changes caused by the volume created by the hydraulic fracture, water injection, and oil production were calculated. The Hoek-Brown failure criterion was used to compute rock-failure potential.

Our numerical results for a waterflooding example show that during water injection, the synergistic effects of reservoir cooling and pore-pressure increase significantly promote rock failure, potentially reactivating healed natural macrofractures and/or creating new macrofractures, especially near an injector. The rock cooling can create small microfractures on the surface of the matrix blocks. In shale oil reservoirs, the numerical experiments indicate that stress changes during water injection can improve oil recovery by opening some of the old macrofractures and creating new small microfractures on the surface of the matrix blocks to promote shallow water invasion into the rock matrix. Furthermore, the new microfractures provide additional interface area between macrofractures and matrix to improve oil drainage when using surfactant and CO_2 enhanced-oil-recovery techniques. These positive effects are particularly important farther away from the immediate vicinity of the hydraulic fracture, which is where much of the undrained oil resides.

Introduction

Waterflooding has been an effective IOR process for decades. However, stress induced by changes in pressure or temperature during waterflooding is typically overlooked or not adequately reported. Water injection changes the stress field in the reservoir and the surrounding rocks by changes in pore pressure and reservoir temperature. For instance, the change in stress within a reservoir can be estimated with the following equation for isotropic rock.

$$\sigma_h - \alpha p = \frac{\upsilon}{1-\upsilon}(\sigma_v - \alpha p) + \frac{E}{1-\upsilon^2}(\varepsilon_h + \upsilon\varepsilon_H) + \frac{E}{1-\upsilon}[\beta(T-T_0)] \quad \cdots\cdots (1)$$

In Eq. 1, σ_h and σ_v are the minimum horizontal and vertical stresses, respectively; α is Biot's coefficient; β is the linear thermal expansion; ν is Poisson's ratio; p is pore pressure; T is temperature; T_0 is initial temperature; and ε_h and ε_H are the strain in the minimal- and maximal-horizontal-stress directions, respectively.

The first term on the right side of Eq. 1 is the contribution from the vertical stress to the effective-horizontal-stress change. The second term is the contribution of the horizontal mechanical strain, and the last term is the contribution from the thermal strain. By use of the classical uniaxial-strain assumption, we drop the second term of Eq. 1, which yields the following equation:

$$\sigma_h - \alpha p = \frac{\upsilon}{1-\upsilon}(\sigma_v - \alpha p) + \frac{E}{1-\upsilon}[\beta(T-T_0)]. \quad \cdots\cdots (2)$$

With Eq. 2, we can derive the following equations, which represent the change in effective stresses as a function of the change in pore pressure and reservoir temperature:

$$(\sigma'_h - \sigma'_{h0}) = -\frac{\upsilon}{1-\upsilon}\alpha(p-p_0) + \frac{E}{1-\upsilon}\beta(T-T_0) \quad \cdots\cdots (3)$$

$$(\sigma'_v - \sigma'_{v0}) = -\alpha(p-p_0), \quad \cdots\cdots (4)$$

where p_0 is the initial reservoir pressure, $\sigma'_h = \sigma_h - \alpha p$, and $\sigma'_{h,0} = \sigma_{h,0} - \alpha p_0$.

As for an application of Eq. 3, consider the following example. Suppose we inject cold water into a reservoir such that the increase in pore pressure is 1,000 psia, whereas the decrease in temperature within the drainage volume of the well is 50°F. The data pertinent to this problem are the following: $\alpha = 0.8$, $\nu = 0.2$, $E = 2.83 \times 10^6$ psi (18 GPa), and $\beta = 5.56 \times 10^{-6}\,°F^{-1}$ ($10^{-5}K^{-1}$).

The change in effective horizontal stress because of pore-pressure increase of 1,000 psia is −200 psia, and the effect of cooling by 50°F is −912 psia, for a net effective-horizontal-stress change of −1,112 psia. The effective-vertical-stress change is −800 psi. The Mohr diagram, **Fig. 1,** shows that the synergistic effects of reservoir cooling and pore-pressure increase promote rock failure, potentially reactivating healed natural fractures and creating new microfractures.

A recent waterflood pilot test in the Viewfield Bakken by Crescent Point Energy (Wood and Milne 2011) indicates improved oil production. The first pilot test included four horizontal producers and one horizontal injector, drilled parallel to each other with well spacing of approximately 656 ft (200 m) **(Fig. 2a).** The first pilot saw a robust production response through the latter part of 2008 and into much of 2009, as shown in Fig. 2b. After reaching a peak production rate of approximately 550 B/D, production declined by approximately 25% over the next 2 years. This decline rate is a great improvement over the 70-to-75% rate decline in the first year of a typical declining rate in the Viewfield Bakken wells (Wells 2011).

Crescent Point Energy also conducted a tracer test. The results indicated immediate water breakthrough to the offset producers. This is not a surprise because injected water tends to flow through the fracture networks created by hydraulic fracturing, displacing the oil toward the production well, and bypassing tight shale matrix, rapidly reaching producers.

We believe that water-injection-induced stress enhances permeability of existing healed natural fractures and creates new

This paper (SPE 158053) was accepted for presentation at the SPE Annual Technical Conference and Exhibition, San Antonio, Texas, USA, 8–10 October 2012, and revised for publication. Original manuscript received for review 18 June 2012. Revised manuscript received for review 26 November 2012. Paper peer approved 16 January 2013.

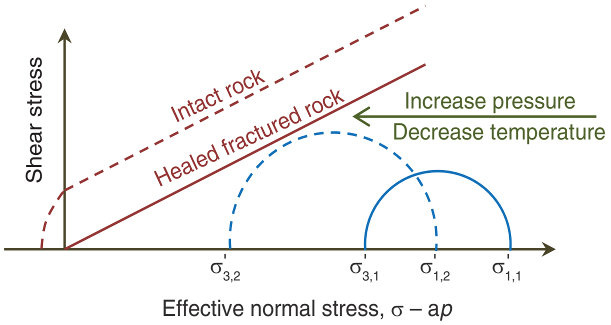

Fig. 1—Mohr diagram for stress change during water injection.

microfractures penetrating into tight matrix rock. These microfractures create flow paths for hydrocarbons inside the matrix, thus improving the fracture/matrix interface area and increasing hydrocarbon production from the matrix. In addition, the principal mechanism of oil displacement by waterflooding is mainly by viscous displacement of oil from the microfractures and possibly with a little contribution from the matrix. The theoretical support for this conclusion will be provided in a future publication.

Because waterflooding appears to be a viable IOR technique, in this paper, we further examine the role of waterflood-induced stress to improve oil recovery. We calculate the magnitude of water-injection-induced stress with a coupled flow/geomechanics model.

In addition to the preceding engineering analysis, we present a numerical model to describe how waterflooding improves oil recovery in shale reservoirs. In support of our numerical-modeling study, published experimental data relating to the waterflood-induced stress will be presented and discussed.

Thermal Stimulation in Geothermal Reservoirs

Thermal stimulation has been reported as a successful stimulation technique for geothermal reservoirs (Siratovich et al. 2011). We speculate that this mechanism is also a key to success in a cold-water injection in Bakken. A typical thermal stimulation is conducted by injecting cold water into hot reservoir rock. Three mechanisms are considered for the success: the reopening of old fractures by thermal contraction, the creation of new fractures from temperature-induced stress exerted on reservoir rocks, and the cleaning of debris or mineral deposits from open fractures (Axelsson et al. 2006).

Siratovich et al. (2011) thoroughly review thermal-stimulation application in a number of geothermal fields worldwide. The stimulation could be conducted right after a well is drilled or long after production, and often is cyclic. The treatment could be performed in a short period ranging from hours to days. Thermal cycling with rapid cooling and heating of the wellbore (by injecting cold water and stopping injection) shows positive results enhancing near-wellbore permeability (Kitao et al. 1990; Bjornsson 2004). Siratovich et al. (2011) also conducted experiments to

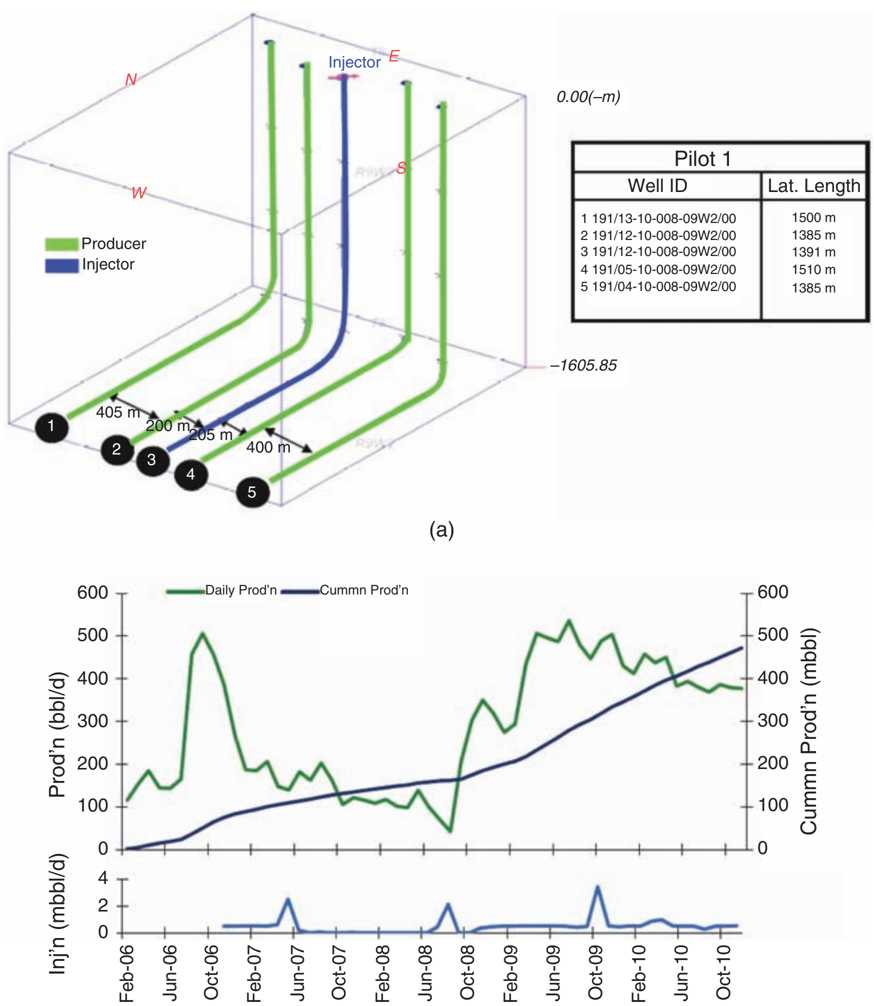

Fig. 2—Waterflooding Pilot Test No. 1 in the Viewfield Bakken by Crescent Point Energy Corporation: (a) well configuration and (b) oil-production and water-injection profiles (Wood and Milne 2011).

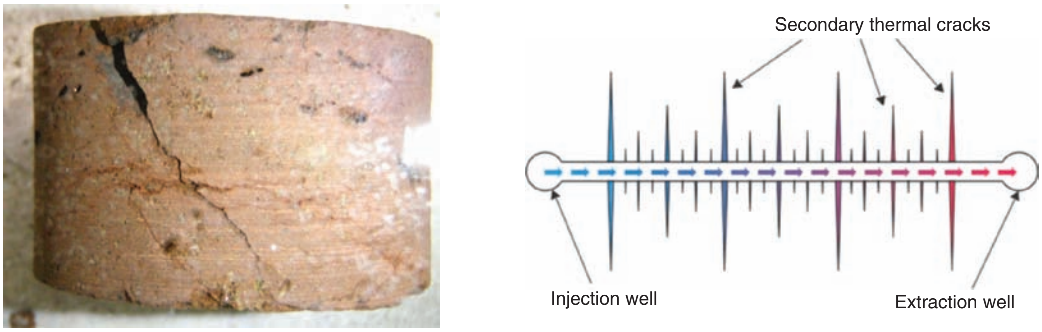

(a) (b)

Fig. 3—Recent studies confirming thermal induced fractures in geothermal reservoirs: (a) an experimental study by Siratovich et al. (2011) showing fracture creation during the experiment on Tjaldfell Tholeiitic basalt specimen by heating the sample to 400°F and immediately submerging it in a 70°F water bath and (b) a numerical study by Ghassemi (2012) showing secondary fractures created by cold-water injection in geothermal reservoirs.

verify that temperature-induced stress can create fractures in a volcanic-rock specimen. The experiment was carried out by heating the specimen to 300 to 650°F and immediately submerging the specimen in a 68°F water bath. Newly created fractures observed on the specimen indicate that temperature-induced stress could create new microfractures **(Fig. 3a).**

Moreover, numerical studies (Ghassemi and Zhang 2004; Ghassemi et al. 2007; Tarasovs and Ghassemi 2012) also illustrate the role of temperature-induced stress to create new fractures. Cold-water circulation in hot fractured rock induces thermal contraction and creates tension near main fractures. Once the induced stress exceeds the rock strength, secondary fractures can propagate from the main fractures (likely perpendicular to them) into matrix rock (Fig. 3b).

We speculate that water-induced microfractures could occur during water injection in the Bakken. These induced microfractures can enhance oil recovery by increasing macrofractures/matrix interface area, thus improving oil production from tight Bakken reservoirs. However, the Bakken reservoir temperature is not as high as that of the aforementioned geothermal reservoirs; it would take a longer period to see the effect of the thermal stimulation. This is consistent with the observations from the water-injection pilot test by Crescent Point Energy. The company indicated that the improvement from water injection could be detected several months to 1 year after starting injection (Wells 2011).

The Research Objective

The objective of this study is to investigate the role of pressure increase and temperature decrease during water injection in the stress redistribution in conventional and unconventional reservoirs and the tendency of water-induced microfractures to form in the Bakken. A coupled flow/geomechanics model is used to calculate pore-pressure- and temperature-induced stress in the reservoirs. In this paper, we conduct two simulation studies: five-spot pattern waterflooding in a conventional reservoir and water injection in a multistage hydraulic-fractured horizontal well in the Bakken.

Mathematical Model for Coupled Flow and Geomechanics

A coupled flow and geomechanics model is used to describe fluid flow, heat transfer, and rock deformation in the formations. This model is built on the basis of the governing equations preserving physical laws (including conservation of mass, momentum, and energy) and constitutive laws (such as Darcy's law, porothermoelasticity, and infinitesimal strain theories). In this paper, we extend the work by Charoenwongsa et al. (2010) to capture a mechanical anisotropic system. Detailed implementation can be found in Charoenwongsa et al. (2010).

Elements of the model include the pore-pressure equation, water-saturation equation, temperature equation, rock-displacement equation, and stress/strain relation.

Pore Pressure Equation.

$$\begin{aligned}&-\nabla\cdot\vec{v}_w-\nabla\cdot\vec{v}_\phi+\hat{q}_t\\&=(1-\varepsilon_v)\phi\left(c_t\frac{\partial p_\phi}{\partial t}-\beta_{fl,t}\frac{\partial T}{\partial t}\right)-\phi\frac{\partial(\nabla\cdot\vec{u})}{\partial t},\quad\cdots\cdots(5)\end{aligned}$$

where $\vec{v}$ is Darcy velocity; $\hat{q}$ is sink and source term per unit volume; subscripts o and w represent the oil and water phases, respectively; ε_v is volume matrix strain; ϕ is porosity; c_t is total compressibility; $\beta_{fl,t}$ is total thermal expansion of fluid; t is time, $\vec{u}$ is the rock displacement vector defined as $\vec{u}=[u,v,w]^T$, and u, v, and w are rock displacement components in the x-, y-, and z-directions, respectively.

Water Saturation Equation.

$$\begin{aligned}&-\nabla\cdot\vec{v}_w+\hat{q}_w\\&=(1-\varepsilon_v)\phi\left\{S_w(c_w+c_\phi)\frac{\partial p}{\partial t}-S_w\beta_{fl,w}\frac{\partial T}{\partial t}+\frac{\partial S_w}{\partial t}\right\}\\&-\phi S_w\frac{\partial(\nabla\cdot\vec{u})}{\partial t}.\quad\cdots\cdots(6)\end{aligned}$$

where c_ϕ and c_w are pore and water compressibility, respectively.

Temperature Equation.

$$\begin{aligned}&-\nabla\cdot\left\{(c_{p,w}\rho_w\vec{v}_w+c_{p,o}\rho_o\vec{v}_o)(T-T^n)\right\}+\nabla\cdot(k_T\nabla T)\\&+\left\{(c_{p,w}\rho_w q_w)(T_{\text{inj}}-T^n)\right\}\\&=\left\{\begin{array}{l}\phi(c_{v,w}\rho_w S_w+c_{v,o}\rho_o S_w)\\+(1-\phi)c_s\rho_s\end{array}\right\}\frac{\partial T}{\partial t},\\&\quad-3\beta K_b T_0\frac{\partial(\nabla\cdot\vec{u})}{\partial t}\quad\cdots\cdots(7)\end{aligned}$$

where ρ is density; c_p is constant pressure heat capacity; c_v is constant-volume heat capacity; subscripts o and w represent the oil and water phases, respectively; c_s is heat capacity of solid, and K_b is drained bulk modulus.

Rock Displacement Equation. X-Direction.

$$\begin{aligned}&\frac{\partial}{\partial x}\left(C_{11}\frac{\partial u}{\partial x}+C_{12}\frac{\partial v}{\partial y}+C_{13}\frac{\partial w}{\partial z}\right)\\&+\frac{\partial}{\partial y}\left(C_{44}\left(\frac{\partial u}{\partial y}+\frac{\partial v}{\partial x}\right)\right)+\frac{\partial}{\partial z}\left(C_{66}\left(\frac{\partial u}{\partial z}+\frac{\partial w}{\partial x}\right)\right)\\&=-\alpha\left(\frac{\partial p_o}{\partial x}-f_w\frac{\partial p_{cwo}}{\partial x}-(f_w\gamma_w+f_o\gamma_o)\frac{\partial D}{\partial x}\right)\\&-\beta(C_{11}+C_{12}+C_{13})\frac{\partial T}{\partial x}\quad\cdots\cdots(8)\end{aligned}$$

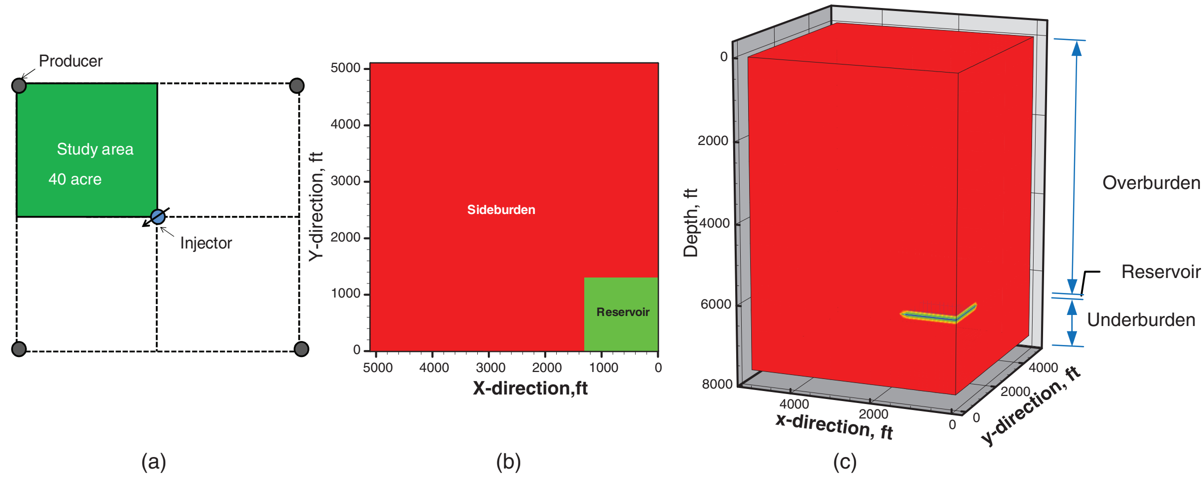

Fig. 4—Model configuration: (a) study area of a quarter-model of a five-spot waterflood pattern; (b) top view of the model reservoir and sideburden; and (c) overburden and underburden layers.

where C_{ij} represents rock mechanical properties defined in a strain/strain relation under drained conditions; detailed calculation is given in Appendix A. p_{cwo} represents capillary pressure of a water/oil system, f is fractional flow, γ is the pressure gradient, and D is depth.

Y-Direction.

$$\frac{\partial}{\partial x}\left(C_{44}\left(\frac{\partial v}{\partial x}+\frac{\partial u}{\partial y}\right)\right)+\frac{\partial}{\partial y}\left(C_{21}\frac{\partial u}{\partial x}+C_{22}\frac{\partial v}{\partial y}+C_{23}\frac{\partial w}{\partial z}\right)$$
$$+\frac{\partial}{\partial z}\left(C_{55}\left(\frac{\partial v}{\partial z}+\frac{\partial w}{\partial y}\right)\right)$$
$$=-\alpha\left(\frac{\partial p_o}{\partial y}-f_w\frac{\partial p_{cwo}}{\partial y}-(f_w\gamma_w+f_o\gamma_o)\frac{\partial D}{\partial y}\right)$$
$$-\beta(C_{21}+C_{22}+C_{23})\frac{\partial T}{\partial y}. \quad \ldots\ldots (9)$$

Z-Direction.

$$\frac{\partial}{\partial x}\left(C_{66}\left(\frac{\partial w}{\partial x}+\frac{\partial u}{\partial z}\right)\right)+\frac{\partial}{\partial y}\left(C_{55}\left(\frac{\partial w}{\partial y}+\frac{\partial v}{\partial z}\right)\right)$$
$$+\frac{\partial}{\partial z}\left(C_{31}\frac{\partial u}{\partial x}+C_{32}\frac{\partial v}{\partial y}+C_{33}\frac{\partial w}{\partial z}\right)$$
$$=-\alpha\left(\frac{\partial p_o}{\partial z}-f_w\frac{\partial p_{cwo}}{\partial z}-(f_w\gamma_w+f_o\gamma_o)\frac{\partial D}{\partial z}\right)$$
$$-\beta(C_{31}+C_{32}+C_{33})\frac{\partial T}{\partial z}. \quad \ldots\ldots (10)$$

The stress/strain relation is

$$\begin{bmatrix}\Delta\sigma_x-\alpha(p-p_0)\\ \Delta\sigma_y-\alpha(p-p_0)\\ \Delta\sigma_z-\alpha(p-p_0)\\ \Delta\tau_{xy}\\ \Delta\tau_{yz}\\ \Delta\tau_{zx}\end{bmatrix}=\begin{bmatrix}C_{11}&C_{12}&C_{13}&&&\\ C_{21}&C_{22}&C_{23}&&&\\ C_{31}&C_{32}&C_{33}&&&\\ &&&C_{44}&&\\ &&&&C_{55}&\\ &&&&&C_{66}\end{bmatrix}$$
$$\times\begin{bmatrix}\varepsilon_x+\beta(T-T_0)\\ \varepsilon_y+\beta(T-T_0)\\ \varepsilon_z+\beta(T-T_0)\\ \varepsilon_{xy}\\ \varepsilon_{yz}\\ \varepsilon_{zx}\end{bmatrix}, \quad \ldots\ldots (11)$$

where $\Delta\sigma_i$ is normal stress change on the i-direction, $\Delta\tau_{ij}$ is shear stress change in the i, j plane, ε_i is normal strain on the i-direction, and ε_{ij} is shear strain on the i, j plane.

For the strain definition, we use the small strain definition, which is mathematically expressed by

$$\varepsilon_x=\frac{\partial u}{\partial x}\ \varepsilon_y=\frac{\partial v}{\partial y}\ \varepsilon_z=\frac{\partial w}{\partial z}$$
$$\varepsilon_{xy}=\frac{1}{2}\left(\frac{\partial u}{\partial y}+\frac{\partial v}{\partial x}\right)\varepsilon_{yz}=\frac{1}{2}\left(\frac{\partial v}{\partial z}+\frac{\partial w}{\partial y}\right)\varepsilon_{zx}=\frac{1}{2}\left(\frac{\partial w}{\partial x}+\frac{\partial u}{\partial z}\right). \quad \ldots\ldots (12)$$

Water-Injection-Induced Stress

Cold-water injection reduces effective stress in reservoirs in two ways, which is evident by reviewing Eq. 1. This equation clearly indicates that the effective stress is reduced when pore pressure increases. Second, the effective stress is reduced when the reservoir cools, which causes rock matrix to contract (volumetric strain). The latter effect is similar to cooling a steel rod with two ends fixed where the volume change caused by thermal contraction creates internal strain in the rod, thus decreasing the stress as well as the effective stress.

To study water-injection-induced stress, we modeled waterflooding in a 160-acre, 50-ft-thick five-spot pattern. Thus, we show the results for only a quarter of this five-spot reservoir segment with injector-to-producer spacing of 1,867 ft. Cold water is injected into the reservoir for 1 year. A coupled fluid-and-heat-flow/geomechanics model based on the work of Charoenwongsa et al. (2010) was used to calculate stress change in the reservoir. **Fig. 4** shows the model configuration with overburden, underburden, and sideburden boundaries. Detailed reservoir data are presented in Appendix B.

Table 1 shows the simulation results for pressure, temperature, and effective-stress changes at various locations. Here, stress change is calculated as the change from the initial condition. Negative stress change indicates reduction of the effective stress. We can see that temperature reduction after 1 year of injection is confined to a range up to 300 ft from the injection well. Thus, the temperature change is relatively slow compared with the pore-pressure change. The contribution of each term on the right side of Eq. 1 to the effective-horizontal-stress change is shown in Table 1. We can clearly see that the stress change at the vicinity of the injector is dominated by thermal strain because of the temperature decrease. The thermal-strain effect reduces farther away from the injector because the temperature reduction occurs only near the injector.

The stress profiles are plotted as the Mohr circle, shown in **Fig. 5a,** including the Mohr-Coulomb failure envelope with a 100-psi cohesion and a friction angle of 30° for healed natural fractures.

TABLE 1—SIMULATION RESULTS OF INDUCED PRESSURE, TEMPERATURE, AND STRESS

Change	At the Injector	200 ft Away From the Injector	300 ft Away From the Injector
Pressure changes, p–p_0 (psi)	895.7	734.9	666.3
Temperature change, T–T_0 (°F)	−114.7	−31.7	−7.3
Effective-stress change in vertical direction, $\sigma'_v - \sigma'_{v0}$ (psi)	−1,395	−626	−456
Mechanical strain in x-direction	0.000172	-3.6×10^{-5}	-5.2×10^{-5}
Mechanical strain in y-direction	0.000172	-3.6×10^{-5}	-5.2×10^{-5}
Effective-stress change in horizontal direction, $\sigma'_h - \sigma'_{h0}$ (psi)	−4,365	−1,621	−653
Effect of the effective-vertical-stress change on the horizontal-stress change (psi)	−465	−209	−152
Effect of the horizontal mechanical strain on the horizontal-stress change (psi)	689	−144	−208
Effect of the thermal strain on the horizontal-stress change (psi)	−4,588	−1,269	−293

On this plot, the intersection of a stress profile and the failure envelope indicates a possible reactivation of healed natural fractures. We can see that the maximum stress reduction is near the injector, where the maximum temperature reduction takes place. The stress and temperature changes become less pronounced farther away from the injector.

Fig. 5b shows a comparison between pore pressure-induced and temperature-induced stress changes at 200 ft from the injector. The pore-pressure increase raises the total stress and causes a slight mechanical strain in the system. This increase reduces effective stress and shifts the Mohr circle to the left. The induced strain creates shear stress and slightly enlarges the Mohr circle. The temperature decrease causes negative strain or tension in the system, and creates significant shear stress caused by the mechanical strain contrast in vertical and horizontal directions. Ultimately, this reduction widens notably and shifts the Mohr circle to the left. Both the pore-pressure increase and the temperature decrease move the Mohr circle toward the failure envelope. In other words, both effects synergistically promote rock failure.

Numerical Simulation of Water Injection in a Sector Model of the Bakken

To evaluate the effect of water injection in a typical Bakken reservoir, a numerical-simulation study for a sector model was carried out. The model represents a reservoir section between a horizontal water injector and an oil producer in the middle Bakken formation. Both wells are assumed to be stimulated by a set of multistage hydraulic fractures, with well spacing of 650 ft, fracture half-length of 150 ft, and fracture spacing of 400 ft (**Fig. 6a).** A typical average hydraulic-fracture width, in shale formation, of 0.2 in. is assumed. The model is initialized when the hydraulic-fracturing job has been completed. Thus, the fracture network created by the hydraulic-fracturing process exists at the start of water injection.

For simplicity, we assume that the fractures network, created as a result of hydraulic fracturing, is parallel with the principal-stress coordinate axes, as shown in Fig. 6c. We realize that the most accurate way to simulate the fractures network is to model the fractures at an angle approximately 20 to 30° from the principal-stress axes. Our approach simplifies computation but it does not detract from the main objective of the research. Fundamentally, we are more interested to know to what extent the pore-pressure and temperature change in the fractures/matrix system affects the stress redistribution in the reservoir. Furthermore, our representation of the microfractures network is amenable to logarithmic-grid distribution, which leads to accurate numerical results (Fig. 6d). Macrofractures were represented by a set of high-permeability orthogonal grid cells with conductivity of 1.0 md-ft in conductivity, compared with 0.002 md-ft for the adjacent matrix grid array.

In this paper, we did not include the mineralization process during water injection. But we suspect that cooling of the formation brine should lead to some mineral precipitation, which can be included in the future research effort.

Overburden and underburden layers are included to capture stress redistribution because of mechanical strain (Fig. 6b). The effect of fracture-face displacement is modeled by applying rock displacement at the boundary of the model, where the hydraulic fractures are. The other lateral and bottom boundaries are assumed zero-displacement, and the surface boundary is modeled by constant-stress boundary (Fig. 6c).

Reservoir and rock-mechanics properties and the initial reservoir conditions are taken from the literature and are summarized in **Appendix B** (Nottenburg et al. 1978; Ye 2010; Kurtoglu et al. 2011; Wang and Zeng 2011). The Bakken reservoir parameters from various authors reported in Appendix B are widely different. Nonetheless, because the main rock-mechanics properties are taken from Wang and Zeng (2011), we used the information from the latter for consistency.

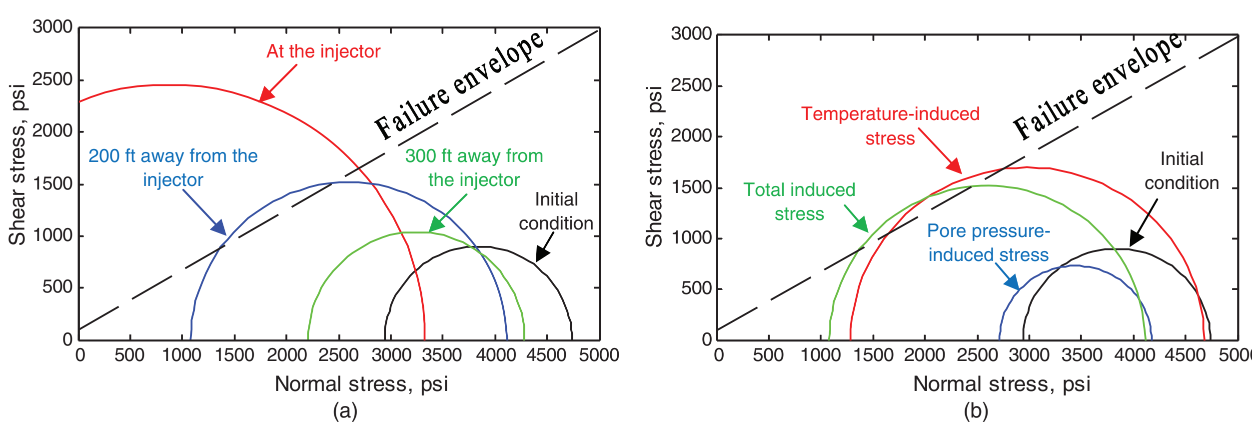

Fig. 5—Simulation results of stress changes after 1 year of injection: (a) effective-stress profile at several locations and (b) comparison between temperature- and pore-pressure-induced stress at 200 ft away from the injector.

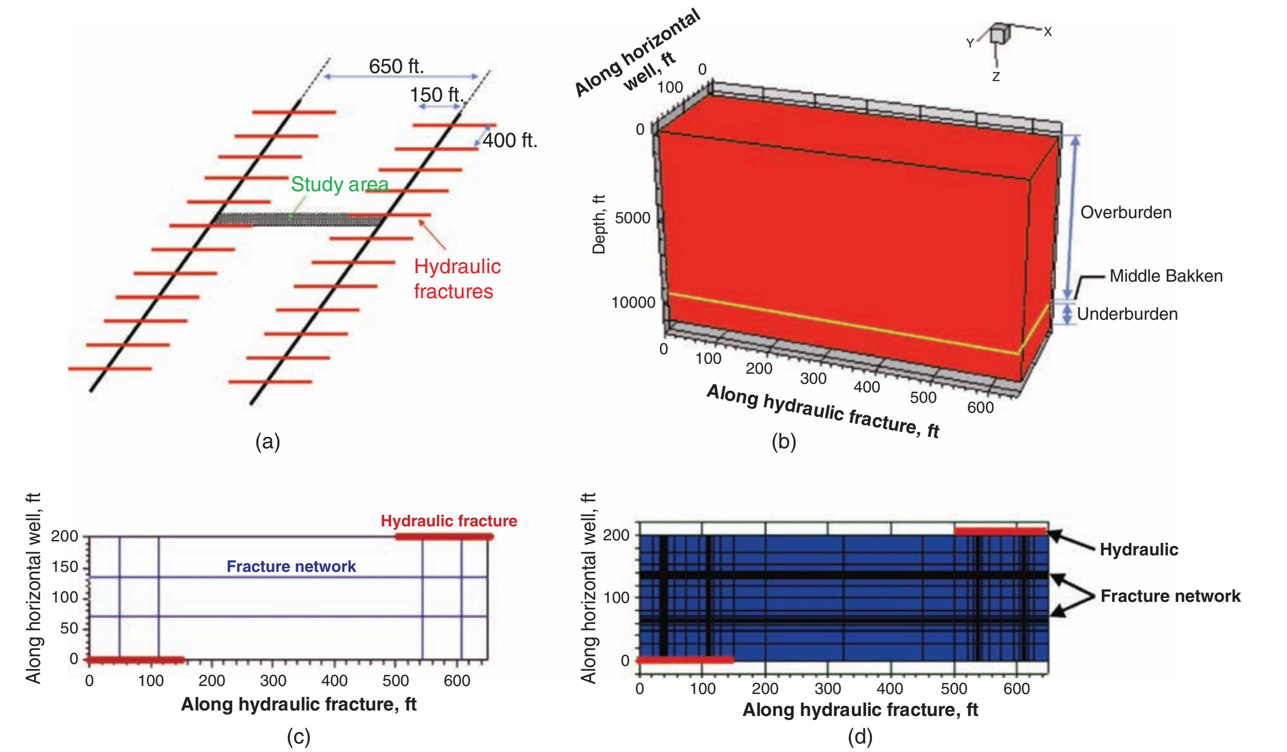

Fig. 6—A sector model for water-injection study in Bakken: (a) schematic of two multistage hydraulically fractured horizontal wells; (b) schematic of the numerical-model configuration for the reservoir sector and surrounding rocks; and (c) the location of the hydraulic fractures, and (d) a natural fracture network in the middle Bakken.

The middle Bakken is modeled by an isotropic material model, but the upper and lower Bakken are transversely anisotropic material. Ye (2010) shows that the mechanical properties of the middle Bakken can be represented as an isotropic material, but the upper and lower Bakken are transversely anisotropic in the principal directions parallel and perpendicular to the bedding. Vernik and Landis (1996) describe the Bakken formation as a sequence of thin layers where silty kerogen-depleted shale layers alternate with kerogen-rich coal-like layers.

Rock Failure

Rock failure occurs when shear stress circle crosses the Mohr-Coulomb or Hoek-Brown failure envelope. Pore-pressure increase and temperature decrease create stress redistribution in the reservoir-rock matrix, which could induce shear failure. Although temperature decrease has the tendency to create tensile failure, the combination of pore-pressure and temperature change would induce shear failure. In this paper, we used the Hoek-Brown failure envelope as the criterion for shear failure.

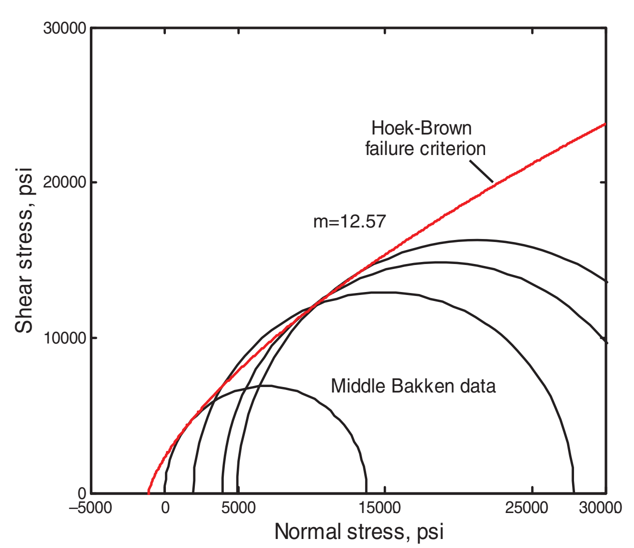

Fig. 7—Hoek-Brown failure criterion best fit for a middle Bakken triaxial test.

When shear failure occurs, it induces a microseismic event for a fast-slip failure (Zoback et al. 2012). On the other hand, a slow-slip failure could take place but will not create a detectable microseismic event. The shear failure is likely to create a large permeability enhancement. Zoback et al. (2012) reported that the main parameters controlling fast- and slow-slip failures are rock mechanical properties and fracture orientation. High clay and/or organic-material content tends to create a ductile behavior, which is likely to deform rather than break. Thus, shear failure in a high-clay-content (more than 30%) formation is likely to produce slow slip, leading to no detectable microseismic signal.

The Hoek-Brown failure criterion is given as (Parry 2004)

$$\sigma'_{1N} = \sigma'_{3N} + \sqrt{m\sigma'_{3N} + Q}, \quad \text{(13)}$$

where σ'_{1N} and σ'_{3N} are normalized maximum and minimum stress defined as σ'_1/σ_c and σ'_3/σ_c, respectively; σ_c is unconfined compressive strength; m is Hoek-Brown fitting parameter; Q is rock quality ranging from 0 for jointed rock masses to 1.0 for intact rock; and σ_c is equal to σ_1 when σ_3 is zero.

By rearranging Eq. 13, we can define a new parameter to characterize rock failure:

$$HB = \sigma'_{1N} - \sigma'_{3N} - \sqrt{m\sigma'_{3N} + 1}, \quad \text{(14)}$$

where HB is the rock-failure indicator for the Hoek-Brown criterion. A positive HB indicates rock failure.

Hoek-Brown failure criterion can be plotted on the Mohr diagram with equations described by Parry (2004):

$$\tau_N = (\cot\phi'_i - \cos\phi'_i)\frac{m}{8}, \quad \text{(15)}$$

where τ_N is the normalized shear stress defined as τ/σ_c and ϕ'_i is the instantaneous friction angle given as

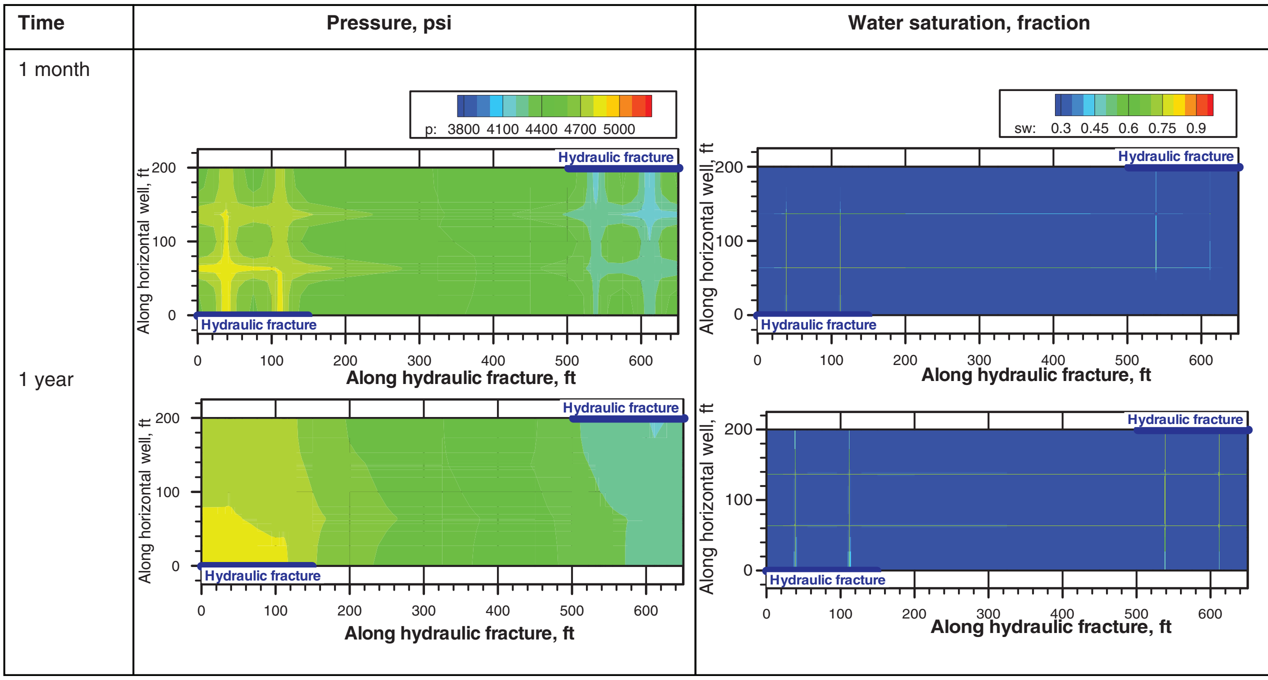

Fig. 8—Simulation results: pressure and water-saturation profiles 1 month and 1 year after cold-water injection.

$$\phi_i' = \tan^{-1}\left[4h\cos^2\left(30^\circ + \frac{1}{3}\sin^{-1}h^{-3/2}\right) - 1\right]^{-1/2}.$$

$$h = 1 + \frac{16(m\sigma_{nN}' + 1)}{3m^2}$$

We used a published triaxial test for the middle Bakken formation (Wang and Zeng 2011) to calibrate the model **(Fig. 7).** The matched parameter, m, is 12.57. This model was used to analyze the simulation results in the next section.

Simulation Results

Fig. 8 shows the simulated pressure and water-saturation distributions during water injection. One month after injection, pressure increases mainly in the fracture network. Later, pressure propagates into tight shale matrix. However, the saturation map indicates that injected water flows overwhelmingly through the fracture network because the shale matrix is so tight and only minimal water can penetrate into the matrix block. In addition, the injected water reaches the producer before 1 month after injection. This is consistent with observations in the Crescent Energy Point (Wells 2011) field pilot experiments.

Fig. 9 depicts the temperature profiles and the vertical-stress change. Temperature reduction occurs at the vicinity to the fracture network near the injector because energy flux from the reservoir causes injected water to heat up, thus there is less cooling effect when it flows deep into the reservoir. After 1 year of injection, the cooling effect takes place inside the tight shale matrix although the injected water cannot penetrate into the matrix, as

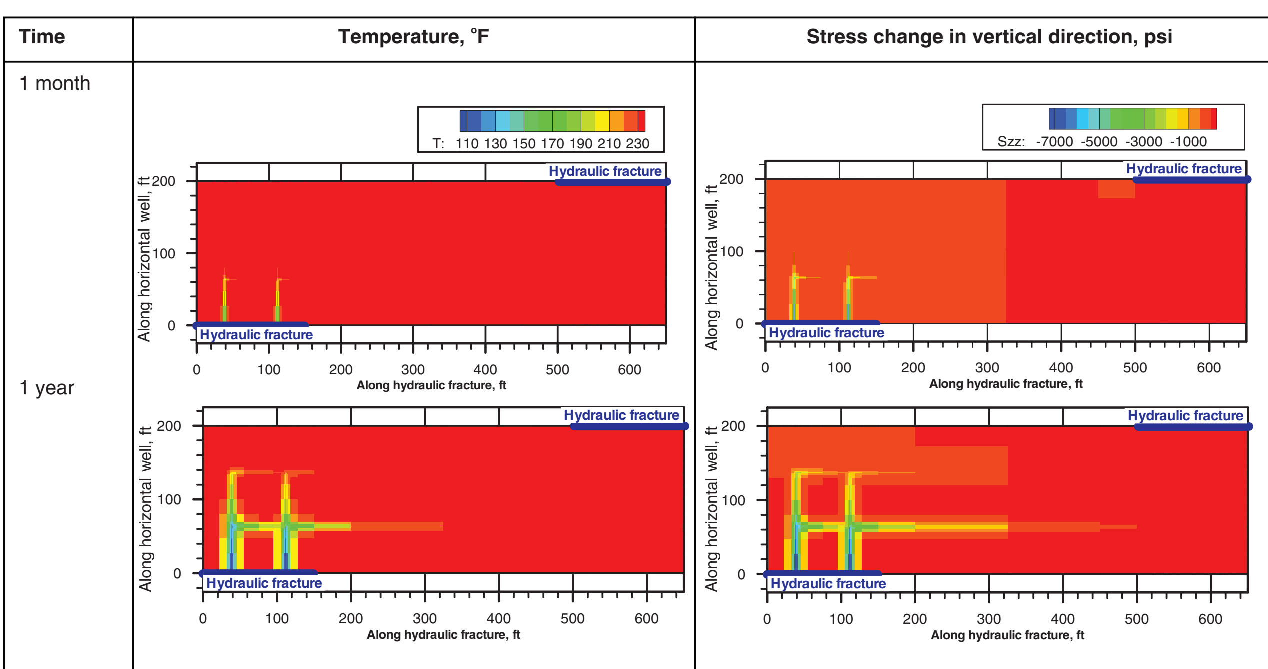

Fig. 9—Simulation results: Temperature and stress changes in the vertical direction 1 month and 1 year after cold-water injection.

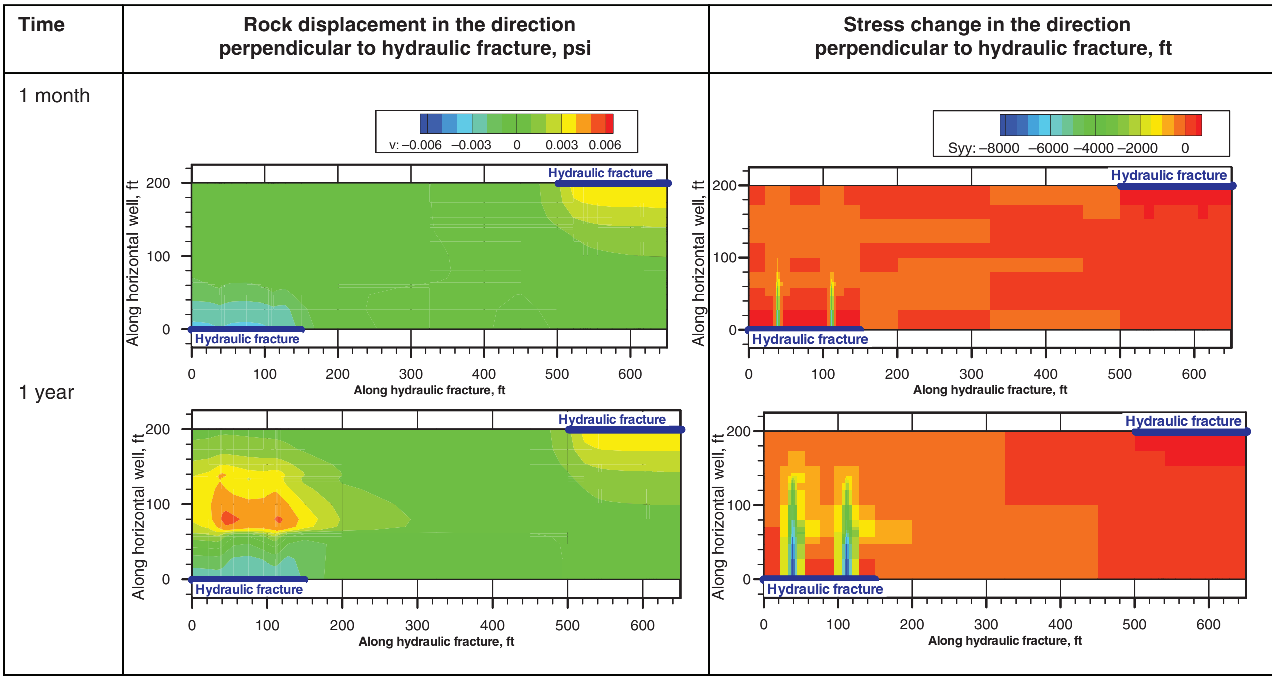

Fig. 10—Simulation results: Rock displacement and stress changes in the direction perpendicular to the hydraulic fracture 1 month and 1 year after cold-water injection.

evidenced in the water-saturation profiles. This cooling effect is dominated by heat conduction, which gradually transfers energy from inside the shale matrix to the fracture network.

The vertical-stress profile indicates that the temperature change exerts much more effect on the stress change than does the pore-pressure change. This is because pressure-change magnitude is relatively small as the reservoir is injected and produced simultaneously. On the other hand, the temperature difference between the injected water and the reservoir is significant and can cause extensive stress change.

Fig. 10 shows the rock displacement and stress change in the minimum-horizontal-stress direction perpendicular to the hydraulic fractures. The hydraulic-fracture-face displacement causes rock displacement and mechanical strain. It increases the effective stress caused by compaction. The stress-change magnitude is relatively small compared with that of pressure and temperature because the typical fracture width of a hydraulic fracture in shale reservoirs is narrow. In this modeling study, we assume the fracture width of 0.2 in., which caused a stress buildup of a few hundred psi. After 1 year, the cooling effect creates contraction, thus reducing the compaction. We can see that the temperature change influences the stress change in the minimum-horizontal-stress direction.

Rock-failure indication calculated from Eq. 6 is plotted in **Fig. 11.** The positive failure indication illustrates rock-failure potential. It can be seen from the plot that the failure potential revolves around the area where the cooling effect takes place. The results confirm the crucial effect of temperature-induced stress on water injection process in the Bakken.

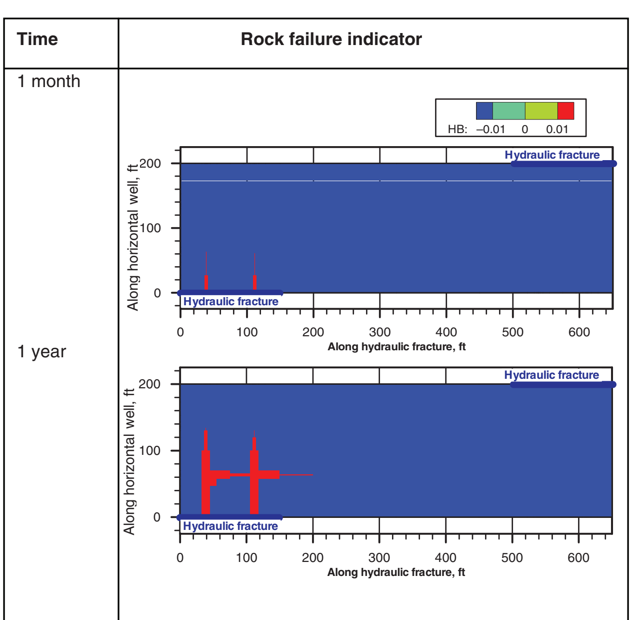

Fig. 11—Simulation results: Likely rock failure sites 1 month and 1 year after cold-water injection.

Improved Hydrocarbon Recovery by Water Injection in Shale Reservoirs

Water injection significantly reduces effective stress, especially with cold-water injection into deep or high temperature formations such as the Bakken, as discussed in the previous section. The reduction could improve hydrocarbon recovery in three respects. First, it could maintain or even improve permeability of existing natural fractures. Second, it could create new microfractures penetrating from the fracture surface into a tight matrix block, creating flow paths and help produce hydrocarbons from the matrix. Finally, injected water could displace hydrocarbons in newly created microfractures.

The proposed process is shown in **Fig. 12.** Initially (Fig. 12a), liquid hydrocarbon situates inside both fracture and shale matrix, where fractures provide main flow paths and matrix contains the majority of hydrocarbons. Once water injection starts (Fig. 12b), the injected water flows only through fracture networks. This was observed in the tracer-testing results during water injection in the Bakken, where Crescent Point Energy found immediate water breakthrough during the test.

The injected water helps maintain pore pressure inside natural fractures and lower temperatures (Fig. 12c) in the matrix surrounding the fractures, thus reducing effective stress on the fractures. **Fig. 13** shows laboratory results (Cuisiat et al. 2002) for permeability of fractures as a function of stress. The reduction of

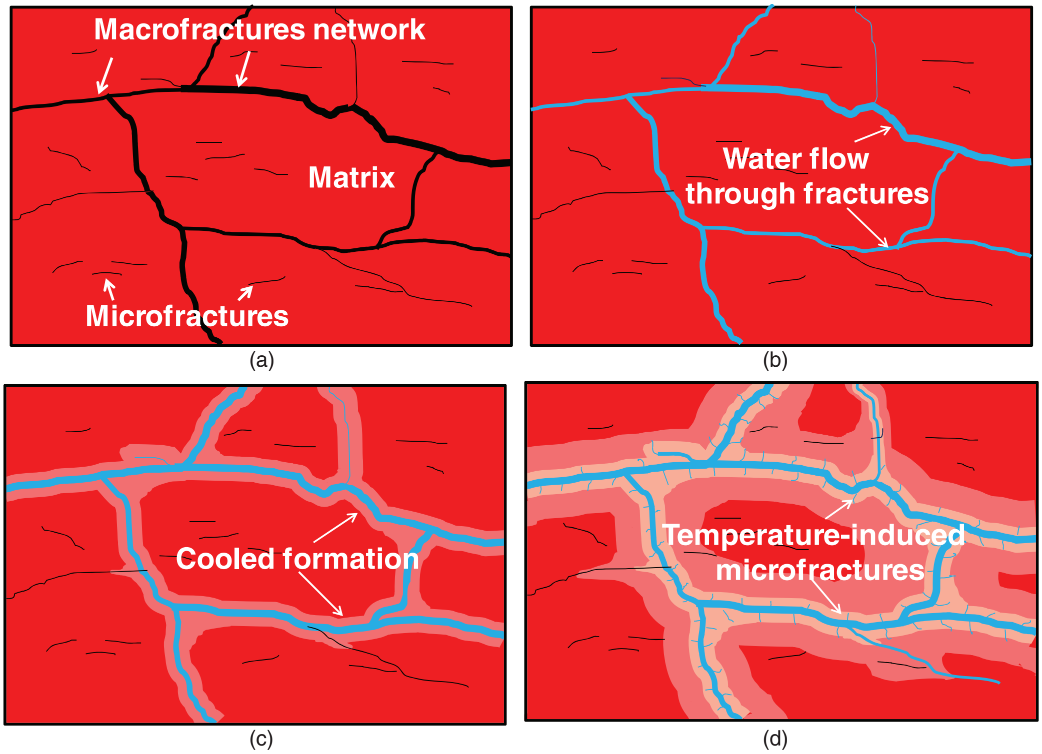

Fig. 12—Enhanced-hydrocarbon-recovery sites resulting from cold-water injection in shale reservoirs: (a) initial condition, (b) early water-injection period where injected water flows only through the fracture network, (c) shale matrix block cooled, and (d) microfractures caused by temperature-induced stress.

effective stress yields fracture-permeability enhancement and vice versa. It is worth mentioning that typical production in shale reservoirs with natural depletion yields high production-rate decline at early production stages, which could be caused by fracture-permeability reduction as pore pressure in fractures is depleted.

The cooling effect induces contraction and creates tension at the vicinity of fractures. Once the stress on the surface of matrix exceeds its strength (Fig. 12d), microfractures are formed from the fracture surface into the matrix block. This could happen months after injection because temperatures gradually change during water injection. These microfractures create flow paths for hydrocarbons inside the matrix, thus improving the fracture/matrix interface area and increasing hydrocarbon production from the matrix.

Fig. 14 shows the experiment conducted by Groisman and Kaplan (1994), in which they investigated the formation of fractures during desiccation. During the process, the specimens lost their water content and contracted, creating tension and forming fractures. The process is generally applicable to the cooling effect that occurs during water injection in shale reservoirs.

Moreover, shale material is prone to failure when exposed to temperature variation. **Fig. 15** shows the experiment conducted by Fu et al. (2004). They observed the influence of heterogeneity on fracture creation during temperature elevation. The results indicated that heterogeneity promotes fracture creation during temperature alterations. Different materials have different thermal-expansion properties. Raising or reducing temperature creates

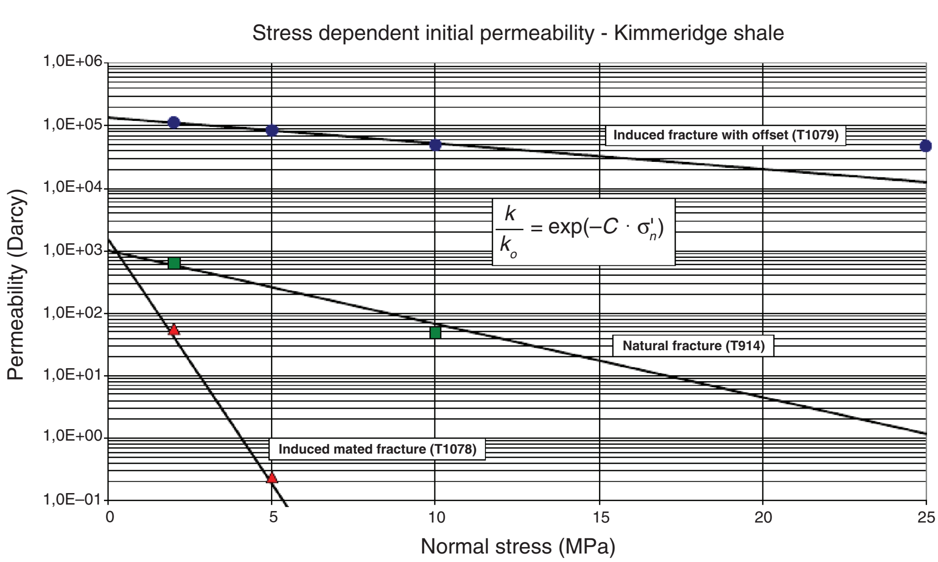

Fig. 13—Decay of North Sea Kimmeridge shale permeability under varied effective normal stress (Cuisiat et al. 2002).

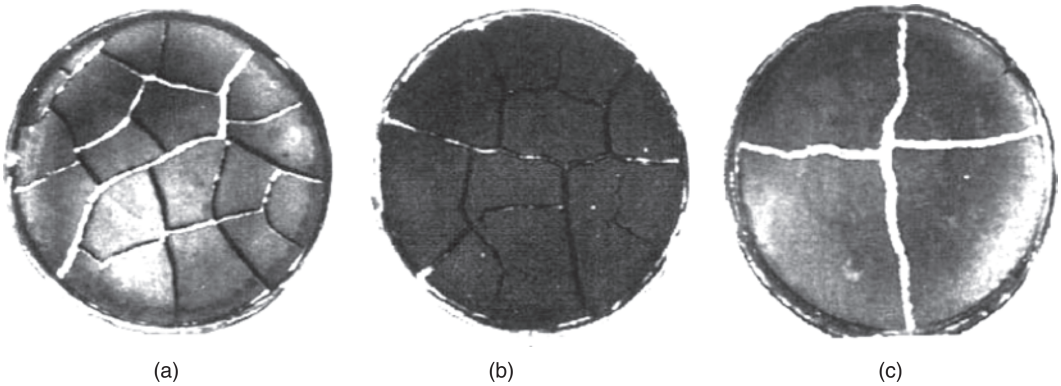

Fig. 14—Pictures of an experiment conducted by Groisman and Kaplan (1994) to investigate fracture creation during desiccation. The pictures show the influence of the bottom friction on the size and pattern of created fractures: (a) glass plate, uncoated; (b) bottom coated with 2 mm of grease; and (c) bottom coated with 6 mm of Vaseline. In our case, created microfractures could be similar to (a) creating small fractures with tight fracture spacing. This is because surface of matrix is under tension caused by cooling effect; its interior, however, is still at its initial condition.

strain contrasts between the two connected materials. This mismatch strain can create internal shear stresses and promote fracture creation. Shale is typically heterogeneous and comprises different materials, such that it is prone to mismatched strains, creating fractures during temperature changes.

Conclusions

We developed a practical numerical model that can be used to study the effect of pore-pressure change and temperature change during water injection on stress redistribution in the reservoir and the surrounding rocks. Such stress changes have many implications, some of which are summarized in the following conclusions.

In conventional waterflooding, reservoir cooling and pore-pressure increase synergistically promote rock failure, potentially reactivating healed natural macrofractures and/or creating new macrofractures, especially near an injector. The rock cooling can create small microfractures on the surface of the matrix blocks.

In shale oil reservoirs, the numerical experiments indicate that stress changes during water injection can improve oil recovery by opening some of the old macrofractures and creating new microfractures perpendicular to the surface of the matrix blocks to promote shallow water invasion into the rock matrix. Then, oil will be produced from the matrix by countercurrent flow into the fractures, where water will displace the oil from the fractures toward the production wells.

The new microfractures provide additional interface area between macrofractures and matrix to improve oil drainage with surfactant and CO_2 enhanced-oil-recovery techniques. These positive effects are particularly important farther away from the immediate vicinity of the hydraulic fracture, where much of the undrained oil resides.

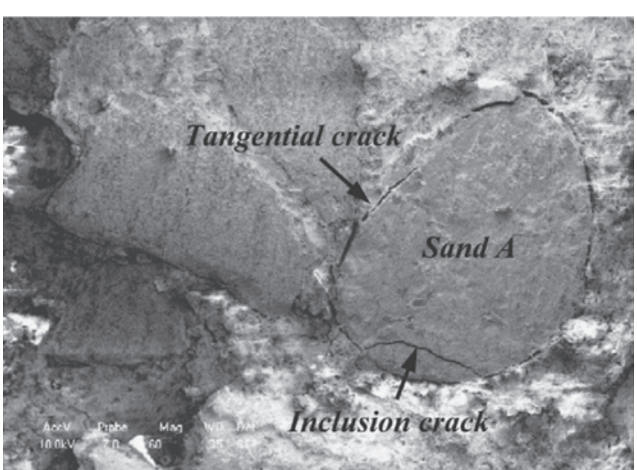

Fig. 15—A picture of an experiment conducted by Fu et al. (2004) to investigate the influence of heterogeneity on fracture creation during temperature elevation. Fractures typically form between two different materials because the strain mismatch of the two materials can create internal shear stress and promote fracture creation.

Nomenclature

c_p = constant pressure heat capacity
c_s = heat capacity of solid
c_t = total compressibility, 1/psi
c_v = constant volume heat capacity
c_ϕ = pore compressibility, 1/psi
C_{ij} = rock mechanical properties defined in strain/strain relation under drained condition
D = depth, ft
f = fractional flow, dimensionless
K_b = drained bulk modulus, psi
m = Hoek-Brown fitting parameter, dimensionless
p = pore pressure, psi
$\hat{q}$ = sink and source term per unit volume, 1/d
Q = rock quality, dimensionless
S = phase saturation, dimensionless
t = time, days
T = temperature, T, °R
T_0 = initial temperature, °F
$\vec{u}$ = rock displacement vector defined as $\vec{u} = [u, v, w]^T$
u, v, w = rock-displacement components in the x-, y-, and z-directions, ft
$\vec{v}$ = Darcy velocity, ft/d
α = Biot's poroelastic constant or effective-stress coefficient, dimensionless
β = coefficient of linear thermal expansion, 1/°F
$\beta_{fl,t}$ = coefficient of total thermal expansion of fluid, 1/°F
γ = pressure gradient, psi/ft
$\Delta\sigma_i$ = normal stress change in i-direction
$\Delta\tau_{ij}$ = shear stress change in i, j plane
ε_i = normal strain on i-direction
ε_{ij} = shear strain on i, j-plane
ε_v = volume matrix strain, dimensionless
ρ = density, lbm/ft^3
σ = stress, psi
σ' = effective stress, psi
σ_c = unconfined compressive strength, psi
υ = Poisson's ratio, dimensionless
ϕ = porosity, dimensionless
ϕ'_i = instantaneous friction angle, degrees

Subscripts

o = oil phase
w = water phase

Acknowledgments

This work is supported by the US Department of Energy under contract No. DE-EE0002762. Special thanks to Energy Modeling Group and Marathon Center of Excellence for Reservoir Studies at Colorado School of Mines.

References

Axelsson, G., Thorhallsson, S., and Bjonsson, G. 2006. Stimulation of Geothermal Wells in Basaltic Rock in Iceland. Proc., ENGINE-Enhanced Geothermal Innovative Network for Europe Workshop, Zurich, Switzerland.

Bjornsson, G. 2004. Reservoir Condition at 3–6 km Depth in the Hellissheidi Geothermal Field, SW-Iceland, Estimated by Deep Drilling, Cold-Water Injection and Seismic Monitoring. Proc., the 29th Stanford Geothermal Workshop, Stanford University, Stanford, California.

Charoenwongsa, S., Kazemi, H., Miskimins, J., et al. 2010. A Fully-Coupled Geomechanics and Flow Model for Hydraulic Fracturing and Reservoir Engineering Applications. Paper SPE 137497 presented at the Canadian Unconventional Resources & International Petroleum Conference, Calgary, Alberta, Canada, 19–21 October.

Cuisiat, F., Grande, L., and Høeg, K. 2002. Laboratory Testing of Long Term Fracture Permeability in Shales. Paper SPE 78215 presented at the SPE/ISRM Rock Mechanics Conference, Irving, Texas, 20–23 October. http://dx. doi.org/10.2118/78215-MS.

Fu, Y.-F., Wong, Y.-L., Poon, C.-S., et al. 2004. Experimental Study of Micro/Macro Crack Development and Stress-Strain Relations of Cement-Based Composite Materials at Elevated Temperatures. *Cement Concrete Res.* **34** (5): 789–797. http://dx.doi.org/10.1016/j.cemconres.2003.08.029.

Ghassemi, A. 2012. A Review of Some Rock Mechanics Issues in Geothermal Reservoir Development. *Geotech. Geol. Eng.* **30** (3): 647–664. http://dx.doi.org/10.1007/s10706-012-9508-3.

Ghassemi, A., Tarasovs, S., and Cheng, A. H.-D. 2007. A 3-D Study of the Effects of Thermomechanical Loads on Fracture Slip in Enhanced Geothermal Reservoirs. *Int. J. Rock Mech. Min.* **44** (8): 1132–1148. http://dx.doi.org/10.1016/j.ijrmms.2007.07.016.

Ghassemi, A. and Zhang, Q. 2004. Poro-Thermoelastic Mechanisms in Wellbore Stability and Reservoir Stimulation. Twenty-Ninth Workshop on Geothermal Reservoir Engineering, Stanford University, Stanford, California, 26–28 January.

Groisman, A. and Kaplan, E. 1994. An Experimental Study of Cracking Induced by Desiccation. *Europhys. Lett.* **25** (6): 415–420. http://dx.doi.org/10.1209/0295-5075/25/6/004.

Kitao, K., Ariki, K., Hatakeyama, H., et al. 1990. Well Stimulation Using Cold-Water Injection Experiments in the Sumikawa Geothermal Field, Akita Prefecture, Japan. Proc., 1990 International Symposium on Geothermal Energy: Geothermal Resources Council 1990 Annual Meeting, Kailua-Kona, Hawaii, Vol. 14, 1219–1224.

Kurtoglu, B., Cox, S. A., and Kazemi, H. 2011. Evaluation of Long-Term Performance of Oil Wells in Elm Coulee Field. Paper SPE 149273 presented at the Canadian Unconventional Resources Conference, Alberta, Canada, 15–17 November. http://dx.doi.org/10.2118/149273-MS.

Nottenburg, R., Rajeshwar, K., Rosenvold, R., et al. 1978. Measurement of Thermal Conductivity of Green River Oil Shales by a Thermal Comparator Technique. *Fuel* **57** (12): 789–795. http://dx.doi.org/10.1016/0016-2361(78)90141-2.

Parry, R. H. G. 2004. *Mohr Circles, Stress Paths and Geotechnics*, second edition. New York, New York: Spon Press.

Siratovich, P. A., Sass, I., Homuth, S., et al. 2011. Thermal Stimulation of Geothermal Reservoirs and Laboratory Investigation of Thermally-Induced Fractures. Proc., Geothermal Resources Council Annual Meeting 2011, San Diego, California, Vol. 35, 1529–1535.

Tarasovs, S. and Ghassemi, A. 2012. On the Role of Thermal Stress in Reservoir Stimulation. Oral presentation given at the Thirty-Seventh Workshop on Geothermal Reservoir Engineering, Stanford University, Stanford, California, 30 January–February 1.

Vernik, L. and Landis, C. 1996. Elastic Anisotropy of Source Rocks: Implications for Hydrocarbon Generation and Primary Migration. *AAPG Bull.* **80** (4): 531–544. http://dx.doi.org/10.1306/64ED8836-1724-11D7-8645000102C1865D.

Wang, C. and Zeng, Z. 2011. Overview of Geomechanical Properties of Bakken Formation in Williston Basin, North Dakota. Paper ARMA 11-199 presented at the 45th U.S. Rock Mechanics/Geomechanics Symposium, San Francisco, Califonia, 26–29 June.

Wells, P. 2011. Bakken Pilot Success Could See Waterflood Tested in Others Tight Oil Plays, Daily Oil Bulletin, April 19, 2011, http://pdf.dailyoilbulletin.com/110419/dob-letter-2011-04-19.pdf (accessed 10 December 2011).

Wood, T. and Milne, B. 2011. Waterflood Potential Could Unlock Billions of Barrels: Crescent Point Energy: Reported by Dundee Securities Ltd., http://www.investorvillage.com/uploads/44821/files/CPGdundee.pdf (accessed 4 May 2012).

Ye, F. 2010. Sensitivity of Seismic Reflections to Variations in Anisotropy in the Bakken Formation, Williston Basin, North Dakota. MS thesis, University of Texas at Austin, Texas (June 2010).

Zoback, M. D., Kohli, A., Das, I., et al. 2012. The Importance of Slow Slip on Faults During Hydraulic Fracturing Stimulation of Shale Gas Reservoirs. Paper SPE 155476 presented at the SPE Americas Unconventional Resources Conference, Pittsburgh, Pennsylvania, 5–7 June. http://dx.doi.org/10.2118/155476-MS.

Appendix A—Mechanical Properties

Isotropic material can be understood as

$$\begin{bmatrix} C_{11} & C_{12} & C_{13} & & & \\ C_{21} & C_{22} & C_{23} & & & \\ C_{31} & C_{32} & C_{33} & & & \\ & & & C_{44} & & \\ & & & & C_{55} & \\ & & & & & C_{66} \end{bmatrix} = \begin{bmatrix} 2G+\lambda & \lambda & \lambda & & & \\ \lambda & 2G+\lambda & \lambda & & & \\ \lambda & \lambda & 2G+\lambda & & & \\ & & & 2G & & \\ & & & & 2G & \\ & & & & & 2G \end{bmatrix}, \quad \text{(A-1)}$$

where G is shear modulus and λ is the Lamé coefficient.

In orthotropic material, the Young's modulus, shear modulus, and Poisson's ratio are direction dependent. For such material, Eq. 13 takes the form

$$\begin{bmatrix} C_{11} & C_{12} & C_{13} & & & \\ C_{21} & C_{22} & C_{23} & & & \\ C_{31} & C_{32} & C_{33} & & & \\ & & & C_{44} & & \\ & & & & C_{55} & \\ & & & & & C_{66} \end{bmatrix} = \begin{bmatrix} 1/E_x & -\upsilon_{yx}/E_y & -\upsilon_{zx}/E_z & & & \\ -\upsilon_{yx}/E_y & 1/E_y & -\upsilon_{zy}/E_z & & & \\ -\upsilon_{zx}/E_z & -\upsilon_{zy}/E_z & 1/E_z & & & \\ & & & 1/2G_{xy} & & \\ & & & & 1/2G_{yz} & \\ & & & & & 1/2G_{zx} \end{bmatrix}^{-1} \quad \text{(A-2)}$$

where E_i is Young modulus in the i-direction, υ_{ij} is Poisson's ratio in the i, j plane, and G_{ij} is shear modulus in the i, j plane.

Appendix B—Input Data for Numerical-Simulation Studies

See **Tables B-1 and B-2.**

TABLE B-1—FIVE-SPOT WATERFLOOD MODEL

Parameter	Value	Unit	Parameter	Value	Unit
Rock properties			Rock-mechanics properties		
Porosity	0.2	—	Elastic modulus	3×10^6	psi
Vertical permeability	10	md	Poisson's ratio	0.25	—
Horizontal permeability	50	md	Shear modulus	10^6	psi
			Biot's constant	0.8	—
Thermal properties			Linear thermal expansion	10^{-5}	$^\circ F^{-1}$
Rock heat capacity	0.21	Btu/(lbm-°F)			
Rock thermal conductivity	35	Btu/(D-ft-°F)	Initial reservoir conditions		
Rock density	170	lbm/ft^3	Initial pressure	2,700	psi
			Initial temperature	200	°F
Well control			Initial water saturation	0.25	—
Injected temperature	80	°F			
Injection rate	500	B/D	160-acre spacing for full pattern		
			Quarter of five-spot, injector/producer distance is 1,867 ft		

TABLE B-2—A SECTOR MODEL OF WATER INJECTION IN THE BAKKEN

Parameter	Value	Unit	Parameters	Value	Unit
Well Control			Fluid Properties		
Injected temperature	80	°F	Oil		
Total injection rate	1,040	B/D	API gravity[1]	42	°API
Sector injection rate	40	B/D	Viscosity[1]	0.36	—
Maximum injection pressure	5,000	psi	Heat capacity	0.6	Btu/(lbm-°F)
Total production rate	1,040	B/D	Heat conductivity	8.0	Btu/(D-ft-°F)
Sector production rate	40	B/D	Water		—
Minimum production pressure	1,000	psi	Viscosity	0.5	—
			Heat capacity	1.0	Btu/(lbm-°F)
			Heat conductivity	9.0	Btu/(D-ft-°F)
Middle Bakken Rock Properties					
Flow Properties			Rock-Mechanics Properties		
Porosity[1]	0.08	—	Elastic modulus[3]	4.5×10^6	psi
Effective permeability[1]	0.05	md	Poisson's ratio[3]	0.30	—
Matrix permeability	0.001	md	Shear modulus[5]	1.7×10^6	psi
Fracture permeability	150	md	Biot's constant[3]	0.8	—
			Linear thermal expansion	10^{-5}	$^\circ F^{-1}$
Thermal Properties					
Heat capacity	0.21	Btu/(lbm·°F)	Initial Conditions		
Thermal conductivity[2]	16.8	Btu/(D-ft-°F)	Initial pressure[3]	4,500	psi
Density	170	lbm/ft^3	Initial temperature[1]	240	°F
			Initial water saturation	0.25	—
Initial Stress Conditions					
Vertical stress[3]	8,000	psi			
Maximum horizontal stress[3]	6,800	psi			
Minimum horizontal stress[3]	6,000	psi			
Underburden and Overburden Rock Properties					
Flow Properties			Rock-Mechanics Properties in Horizontal Direction		
Porosity	0.01	—	Drained elastic modulus[4]	4.5×10^6	psi
Total permeability	0	md	Poisson's ratio[4]	0.30	—
			Shear modulus[5]	1.7×10^6	psi
Thermal Properties			Biot's constant	0.8	—
Heat capacity	0.21	Btu/(lbm-°F)	Linear thermal expansion	10^{-5}	$^\circ F^{-1}$

TABLE B-2 (continued)—A SECTOR MODEL OF WATER INJECTION IN THE BAKKEN

Parameter	Value	Unit	Parameters	Value	Unit
Thermal conductivity[2]	16.8	Btu/(D-ft-°F)			
Density	170	lbm/ft^3	Rock-Mechanics Properties in Vertical Direction		
			Elastic modulus[3]	6.8×10^6	psi
			Poisson's ratio[3]	0.18	—
			Shear modulus	1.7×10^6	psi
			Biot's constant	0.8	—
			Linear thermal expansion	10^{-5}	$°F^{-1}$

[1] Kurtoglu et al. (2011)
[2] Nottenburg et al. (1978)
[3] Wang and Zeng (2011)
[4] Ye (2010)
[5] Calculated from other mechanical properties.

Perapon Fakcharoenphol is a PhD candidate in petroleum engineering at the Colorado School of Mines (CSM). His research interests are numerical simulation of coupled geomechanics and transport in porous and fractured media. He worked as a reservoir engineer for PTT Exploration and Production Company (PTTEP) from 2002 to 2008. Fakcharoenphol holds an MS degree in petroleum engineering from Imperial College, London, and a BS degree in petroleum engineering from Chulalongkorn University, Thailand.

Sarinya Charoenwongsa is a petroleum engineer at Chevron Energy Technology Company. She worked as a reservoir engineer for PTTEP from 2002 to 2007 and as a post-doctoral research scientist at CSM in 2012. She holds BS and MS degrees in chemical engineering from King's Mongkut Institute of Technology, Ladkrabang, and Chulalongkorn University, respectively. Charoenwongsa holds a PhD degree in petroleum engineering from CSM.

Hossein Kazemi is the Chesebro' Distinguished Professor of Petroleum Engineering at CSM and codirector of the Marathon Center of Excellence for Reservoir Studies (MCERS). Kazemi is a member of the National Academy of Engineering and is an SPE Distinguished Member and Honorary Member. He retired from Marathon Oil Company in 2001 after serving as the Director of Production Research, the Manager of Reservoir Technology, and an executive technical fellow. At CSM, Kazemi teaches graduate courses and supervises research in reservoir modeling, well testing, and improved oil- and gas-recovery processes. He holds BS and PhD degrees in petroleum engineering from the University of Texas at Austin.

Yu-Shu Wu is a professor and Foundation CMG Research Chair in Petroleum Engineering at the CSM. He is also a guest scientist at the earth sciences division of the Lawrence Berkeley National Laboratory (LBNL). At CSM, he is teaching petroleum reservoir engineering courses, supervising graduate students, and conducting research in the areas of multiphase fluid and heat flow in porous media, enhanced-oil-recovery operation, CO_2 geosequestration, reservoir simulation, enhanced geothermal systems, and unconventional hydrocarbon reservoirs. Wu was a staff scientist with the LBNL, from 1995 to 2008. He started his career as a petroleum engineer at RIPED, Beijing. Wu holds BS (Eqv.) and MS degrees in petroleum engineering in China and MS and PhD degrees in reservoir engineering from the University of California at Berkeley.